Economic optimization of a chevron-plate pentane evaporator for a modern high-temperature heat pump

Jussi Saari [1]*, Antti Pitkäoja[1], Antti Uusitalo[1], Satu Lipiäinen[1], Jouni Ritvanen[1]

[1]LUT University, School of Energy Systems, Lappeenranta, Finland

*Corresponding Author: saari@lut.fi

ABSTRACT

This study presents the optimization (capital cost minimization) of a low-pressure brazed plate pentane evaporator for a two-stage 5 MW_{th} heat pump concept for district heat generation using an air collector heat source. Pentane was chosen as the work fluid through requirements for low environmental impact, and centrifugal compressor design constraints. The evaporator operates in a natural-circulation loop with a drum to separate the liquid and vapor phases before the superheater and compressor. The low saturation pressure of pentane at low temperatures and consequent sensitivity of saturated temperature to even very small pressure changes, a highly unusual temperature profile with minimum temperature difference at the middle of the plate is obtained. A Cuckoo Search variant augmented with a modified Hooke-Jeeves search for terminal convergence was used in the optimization. The optimized design consists of two large, 3.8×1.8 meter, evaporators in parallel, with over 300 plates each. Despite the large size, at an estimated 200 000 € cost, the sizing appears technically and economically feasible.

1 INTRODUCTION

In recent years, there has been an increased interest in electrification as a solution for integrating renewable power, such as solar and wind, to heating solutions. Heat pumps represent an energy-efficient way of replacing fossil fuel combustion with renewable electricity for heating. Within heat pump technology, a recent trend is the aim to replace currently common work fluids, which often have high global warming potential (GWP), with low- or zero-GWP fluids (IEA 2022). For example, in EU the new F-gas regulation includes high ambition level for phasing out the use of high GWP fluorinated gases by 2050 (European Commission 2024). The synthetic fluids categorized as hydrofluoro-olefins have low GWP and high stability and have been seen as potential replacements for the previously common high-GWP fluids. However, these fluids are categorized as per- and polyfluoroalkyl substances (PFAS), and they can have negative long-term environmental impacts. The new PFAS-regulation proposal may restrict the use of such fluids in the near future (European Chemicals Agency, 2024). Due to the environmental effects of synthetic refrigerants, natural refrigerants, e.g., different hydrocarbons, CO_2 or ammonia will likely be favored in heat pumps in the future.

This work investigates the design optimization of a plate-type evaporator for a large high-temperature heat pump (HTHP) for an approximately 5 MW_{th} (condenser) air-source heat pump using a two-stage cascade configuration and centrifugal compressors. The heat source is an air collector field heating a stream of water-antifreeze (Freezium) mixture with +5 °C air, while district heating (DH) water serves as the heat sink; this work focuses on the optimization of the evaporator. At the design point for which the chevron-plate evaporator is optimized, the Freezium enters the evaporator at 0 °C to produce 0.15 bar(a), -10 °C pentane. The condenser produces 85 °C DH supply water. The operating conditions were selected based on typical climate conditions and DH temperatures in the Nordic countries.

Pentane was selected as the refrigerant for the heat pump, as among the different natural refrigerants, it allows high COP at the selected conditions, and is also suitable refrigerant for the centrifugal

https://doi.org/10.52202/077185-0108

compressor design, including the compressor efficiency, required rotational speed, and impeller dimensions (Jaatinen-Värri et al. 2024). A drawback of pentane is the very low sub-atmospheric saturation pressure at relevant temperature levels. This makes the boiling point sensitive to even small hydrostatic pressure changes along the plate height.

2 PROBLEM DEFINITION AND OBJECTIVE FUNCTION

Plate heat exchangers are more cost-effective than shell-and-tube heat exchangers when pressures, temperatures and fouling characteristics permit their use. Here, relatively clean fluids at moderate pressures are considered; a brazed plate heat exchanger (BPHE) is thus considered for the application. To evaluate the impact of the low-GWP fluids on heat exchanger design compared to traditional fluids, a design optimization for cost minimization against pressure drop (Δp) and heat rate constraints. For 5 MW_{th} heat output, 3.262 MW evaporator heat rate is required at the design point, where +5 °C air is used to heat a 34% concentration Freezium solution from -8 to 0 °C in an air collector field. The Freezium solution serves as the heat source for the heat pump, whose configuration is shown in Fig.1.

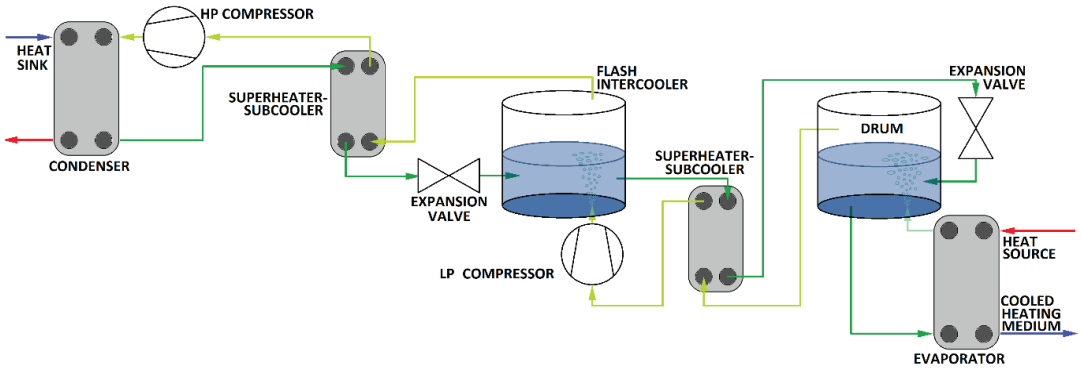

Figure 1: Two-stage heat pump concept.

The subcooler-superheaters are vital for the safe operating environment of the centrifugal compressor: the rotor can be damaged by any liquid droplets in the vapor. The shape of pentane saturated vapor curve results in a risk of compression entering the wet vapor region even if the starting point is in the dry region. The superheater provides a necessary safety margin against this.

2.1 Objective function

The objective function to minimize was the total direct cost C_{DC} of the evaporator unit, consisting of one or a small number of parallel heat exchangers. The C_{DC} was estimated at 3.2 times the purchased equipment costs C_{PE} of a plate heat exchanger (Mendoza *et al.*, 2023). With multiple evaporators, an additional 10 000 € cost penalty was estimated for every additional evaporator. This is still an approximate order-of-magnitude estimate, not yet based on an analysis of the piping, installation, and instrumentation costs. The C_{PE} was estimated from total area A_{tot} with a correlation used in (Mendoza *et al.*, 2023), converted from USD to EUR, and index-corrected from 2020 to the end of 2023 using the producer price index for metal industry products other than machinery (Statistics Finland, 2024) to yield

$$C_{\mathrm{PE,evap}} = 662 + 22.3A_{\mathrm{tot}}^{0.928}. \quad (1)$$

The total heat transfer area A_{tot} is

$$A_{\mathrm{tot}} = L_{\mathrm{tot}} B_{\mathrm{tot}} N_{\mathrm{plt}}, \quad (2)$$

where L_{tot} and B_{tot} are the outer dimensions of a plate, and N_{plt} the number of plates. A conventional chevron plate configuration was considered; the configuration and dimensions are depicted in Fig.2.

https://doi.org/10.52202/077185-0108

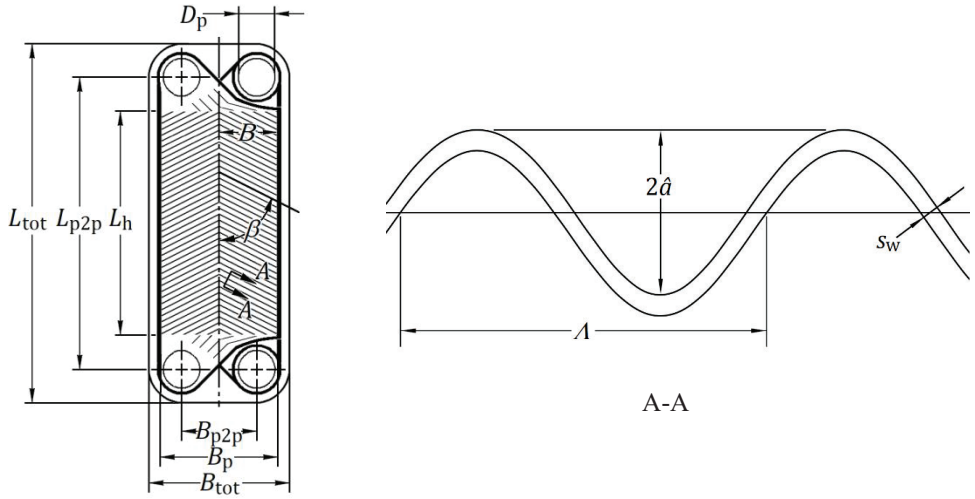

Figure 2: Plate main dimensions.

It should be noted that the effective heat transfer area is less than the total plate area. Heat is only transferred where the plate separates the two fluids. For a conservative estimate, only the main heat transfer area A_h over height L_h is considered. For a single plate, this is

$$A_h = L_h B_p \phi, \tag{3}$$

where $L_h B_p$ is the projection of the area, and ϕ the enlargement factor due to the chevron pattern. In a brazed heat exchanger without gaskets, B_p=B_{tot}. Assuming a typical sinusoidal pattern as in the *A-A* view of Figure 2, ϕ is found using the wave number X,

$$X = \frac{2\pi\hat{a}}{\Lambda} \tag{4}$$

$$\phi(X) \approx \frac{1}{6}\left(1 + \sqrt{1+X^2} + \sqrt{1+\frac{X^2}{2}}\right), \tag{5}$$

where $\hat{a}$ is the sine pattern amplitude, and Λ the wavelength. Eq. (5) represents a 3-point integration over the sine curve length, yielding a ±2% estimate of the enlargement (Martin, 2010).

The problem was formulated with eight decision variables x_n, listed in Table 1 along with the feasible ranges. A vector **x** of eight values defines a candidate solution geometry so that the thermohydraulic performance can be evaluated. In addition to the decision variable box constraints, additional constraints are set to ensure both sufficient performance and limit the search within good design practices and within heat transfer and pressure drop correlation validity regions. These are listed in Table 2. The constraints were set very broad to prevent accidentally ruling out solution space that against expectation would prove viable: e.g. the port velocity maximum of 7 m/s is unlikely to be reached or even approached in any techno-economically viable design, but this was left for the optimizer to determine. A $2 \cdot 10^{-5}$ m^{2}K/W fouling resistance for both Freezium and pentane sides based on Müller-Steinhagen (2010), and 0.4 mm AISI-304L stainless steel plates (thermal conductivity 15 W/mK) are considered.

Fluid properties needed in the thermohydraulic modelling were determined for pentane using the CoolProp thermophysical library. For the Freezium solution, publicly available data tabulated at different temperatures and solution concentrations were used to develop polynomial fits as a function of temperature for each concentration, permitting interpolation between concentrations if necessary.

https://doi.org/10.52202/077185-0108

Table 1: Decision variables and their feasible ranges. Inlet and exit port diameters are identical.

Variable	Explanation	Dimension	Feasible range
x_1	Plate length, L_{tot}	[m]	$0.4 < x_1 < 3.8$
x_2	Plate width, B_{tot}	[m]	$0.1 < x_2 < 2.2$
x_3	Port diameter, fraction of plate width, $D_{\mathrm{p}}/B_{\mathrm{tot}}$	[-]	$0.1 < x_3 < 0.35$
x_4	Chevron angle, β	[°]	$25 < x_4 < 70$
x_5	Chevron wavelength (pitch), Λ	[mm]	$5.0 < x_5 < 50$
x_6	Chevron amplitude, ratio to pitch, $\frac{\Lambda}{\hat{a}}$	[-]	$2.0 < x_6 < 5.0$
x_7	Number of plates, N_{plt}	[-]	$50 < x_7 < 1000$
x_8	Number of parallel heat exchangers, N_{HX}	[-]	$1 < x_8 < 5$

Table 2: Constraints additional to decision variable box constraints.

Constraint	Boundaries
Hot (Freezium) pressure drop	$\Delta p_{\mathrm{h}} < 50$ kPa
Port velocity (liquid)	$w_{\mathrm{p}} < 7\ \mathrm{m/s}$
Port flow (vapour)	$\dot{V} < 10\ \mathrm{m^3/s}$
Plate height/width ratio	$\frac{L_{\mathrm{h}}}{B_{\mathrm{tot}}} > 1.0$

2.2 Heat transfer coefficients

Area A_{h} is found using the fundamental heat exchanger sizing equation as

$$\Phi = UA_{\mathrm{h}} \frac{\Delta T_1 - \Delta T_2}{\ln \frac{\Delta T_1}{\Delta T_2}}, \tag{6}$$

where U is the overall heat transfer coefficient [W/m^{2}K], and ΔT_1 and ΔT_2 the temperature differences between hot and cold fluids at inlet and outlet, respectively. The overall heat transfer coefficient U is

$$U = \left(\frac{1}{h_{\mathrm{h}}} + R''_{\mathrm{tf,h}} + \frac{s_{\mathrm{w}}}{k_{\mathrm{w}}} + R''_{\mathrm{tf,c}} + \frac{1}{h_{\mathrm{c}}} \right)^{-1}, \tag{7}$$

where h_{c} and h_{h} are the cold- and hot-side heat transfer coefficients [W/m^{2}K], R''_{tf} are the thermal fouling resistances [m^{2}K/W], and term $s_{\mathrm{w}}/k_{\mathrm{w}}$ is the thermal conduction resistance through a plate having a thickness of s_{w} [m], and a plate material thermal conductivity of k_{w} [W/mK]. The heat transfer coefficients h are solved by first solving Nusselt number Nu for convection (single-phase fluid heat transfer) or evaporation, and then solving the h from the Nusselt number definition,

$$Nu = \frac{hL}{k_{\mathrm{f}}}, \tag{8}$$

where k_{f} is the thermal conductivity of the fluid in question, and L the characteristic length. In a plate heat exchanger, the characteristic length is in practice always the hydraulic diameter d_{h},

$$d_{\mathrm{h}} = \frac{4\hat{a}}{\phi}. \tag{9}$$

Heat transfer and pressure drop calculation in single-phase flow in a chevron-type plate heat exchanger core is based on Martin (2010), and Martin (1996) as cited by Shah and Sekulic (2003). The Nusselt number is obtained from

$$Nu = 0.205 \left(fRe^2 \sin 2\beta \right)^{0.374} Pr^{1/3} \left(\frac{\mu_{\mathrm{m}}}{\mu_{\mathrm{s}}} \right)^{1/6}, \tag{10}$$

where f is the Fanning friction factor, β the chevron angle (see Figure 2), Re the Reynolds number, Pr the Prandtl number, and μ_{m} and μ_{s} the dynamic viscosities evaluated at the fluid mean bulk temperature and the plate surface temperatures, respectively,

$$Re = \frac{\rho w d_{\mathrm{h}}}{\mu} = \frac{G d_{\mathrm{h}}}{\mu}, \tag{11}$$

https://doi.org/10.52202/077185-0108

where all properties are evaluated at mean bulk temperature, velocity w corresponds to the maximum free flow area for a constant plate spacing of $2\hat{a}$, and G is the similarly defined mass velocity,

$$G = \frac{\dot{m}}{2\hat{a}B_\mathrm{p}}. \tag{12}$$

The f in Eq.(10) is obtained using parameters f_0 and f_1, piecewise-defined as functions of Re:

$$\frac{1}{\sqrt{f}} = \frac{\cos\beta}{\sqrt{0.045\tan\beta + 0.090\sin\beta + \frac{f_0}{\cos\beta}}} + \frac{1-\cos\beta}{\sqrt{3.8 f_1}}, \tag{13}$$

$$Re < 2000 \qquad\qquad Re \geq 2000$$

$$f_0 = \frac{16}{Re} \qquad\qquad f_0 = [1.56(\ln Re) - 3.0]^{-2} \tag{14a}$$

$$f_1 = \frac{149.25}{Re} + 0.9625 \qquad\qquad f_1 = \frac{9.75}{Re^{0.289}} \tag{14b}$$

The correlation is valid for corrugation angles $\beta \in (10°, 80°)$; in this range, for industrial plates, Eq.(13) accuracy is ±40 %, and Eq.(10) ±13 % (Shah & Sekulić, 2003).

The wall temperature for evaluating the value of μ_s Eq.(10) is obtained using thermal circuit and the stationary-state energy balance over the heat transfer surface,

$$\Phi'' = U(T_\mathrm{h} - T_\mathrm{c}) = h_\mathrm{h}(T_\mathrm{h} - T_\mathrm{s,h}) = h_\mathrm{c}(T_\mathrm{s,c} - T_\mathrm{c}), \tag{15}$$

solving for hot- or cold-side surface temperatures $T_\mathrm{s,h}$ or $T_\mathrm{s,c}$, as necessary. As the surface heat transfer coefficients h are both functions of, and components of U, the solution process is iterative.

Predicting boiling heat transfer coefficient accurately in a plate heat exchanger is challenging, with a variety of flow regimes and phenomena taking place; there is a lack of accurate, widely accepted, and applicable correlations for boiling heat transfer in chevron-plate evaporators. Boiling can be broadly divided in pool and flow boiling. In pool boiling, fluid velocity has negligible effect on bubble formation and heat transfer; gravity dominates fluid movement. In practice, even without a forced flow, boiling in a narrow vertical channel rapidly generates sufficient velocity that the pool boiling becomes a poor analogy. Within convective flow boiling, different regimes can be identified. Different phenomena, and properties of the flow, have varying effects at different regimes. Channel size also affects the flow. Kew and Cornwell (1997) suggest the confinement effects are significant when the confinement number Co,

$$Co = \frac{\sqrt{\sigma/[g(\rho_\mathrm{l} - \rho_\mathrm{v})]}}{d_\mathrm{h}}, \tag{16}$$

exceeds 0.5. In Eq.(16), σ is the surface tension [N/m], g the gravitational acceleration, 9.81 m/s^2, and subscripts l and v refer to the saturated liquid and vapor phases, respectively. Instead of Co, its inverse square Bond number Bd can be used, $Bd = Co^{-2}$, with confinement effects significant at $Bd < 4$.

Typically, five or more pre-dryout non-confined boiling regimes are identified (Kakaç, 1991), (Barbosa *et al.*,2007), but Kew & Cornwell (1997) suggest that for confined flows, just three pre-dryout regimes would suffice (Fig. 3). The initial bubble formation is broadly similar in both cases, with heat transfer rates similar to nucleate boiling, but differences apparent as vapor fraction increases.

In large channels boiling transitions through slug and churn flows as bubbles coalesce and interact with each other in an increasingly agitated flow. With still increased vapor fraction the flow transitions to an annular flow with a wavy film at the channel sides. Finally, dry-out leaves liquid only as mist carried in the flow, heat transfer coefficients plummeting towards gas-phase convection values at the dry walls.

Large surface tension and/or small channel size increases bubble size relative to the channel, leading to different, simpler flow patterns in confined flows (Fig.3). Coalescing bubbles quickly span the channel width, and rapid bubble growth may cause pressure fluctuations and instability in multi-channel cases (Kew, 1996). Expanding bubbles push liquid to the sides, forming an annular slug flow with periodic

https://doi.org/10.52202/077185-0108

dry-outs. The last remaining liquid is found irregularly at the surface, not as entrained mist (Kew, 1996). When several phenomena impact the boiling behavior, ideally different correlations should be used to model the heat transfer under different flow regimes (Kakaç, 1991), but in practice, this is unrealistic.

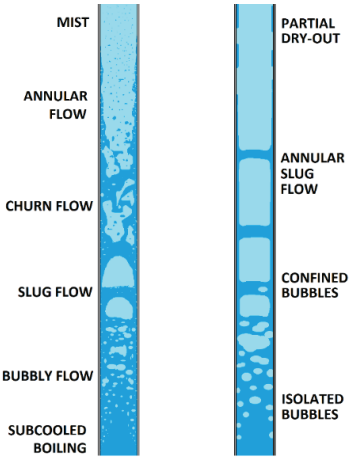

Figure 3: Convection boiling flow regimes depicted in a large, non-confined channel, $Co < 0.5$ (left), and in a small, confined channel with $Co > 0.5$ (right).

Many of the boiling correlations for chevron-plate heat exchangers are specific to one or a few fluids. Specific correlations for pentane could not be found. Two broadly applicable correlations have recently been introduced; one by Longo *et al*. (2015), and the other by Amalfi *et al*. (2016); the latter is used here, defined separately for confined (Co>½,) flows, Eq.(17), and non-confined, Eq.(18), using the dimensionless parameters of Table 3.

$$Nu = 982\,\beta^{*1.101}\,\rho^{*-0.224} We_{\mathrm{m}}^{0.315} Bo^{0.320}, \tag{17}$$

$$Nu = 18.5\,\beta^{*0.248}\,\rho^{*-0.223}\, Re_{\mathrm{v}}^{0.135} Re_{\mathrm{lo}}^{0.351} Co^{0.47} Bo^{0.198}, \tag{18}$$

Table 3: Dimensionless parameters for equations (17) and (18).

Parameter	Equation	Notes
Boiling number *Bo*	$Bo = \frac{\Phi''}{G\,h_{\mathrm{fg}}}$	Ratio of gravitational force to surface tension. Φ'' is heat flux [W/m^2], and h_{fg} the latent heat of evaporation [J/kg].
Confinement number *Co*	$Co = \frac{\sqrt{\sigma/[g(\rho_{\mathrm{l}}-\rho_{\mathrm{v}})]}}{d_{\mathrm{h}}}$	Contained boiling (bubbles large relative to channel) when $Co > 0.5$.
Reynolds number *Re*	$Re = \frac{w d_{\mathrm{h}} \rho}{\mu} = \frac{G d_{\mathrm{h}}}{\mu}$	
- Liquid-only Re_{lo}	$Re_{\mathrm{lo}} = \frac{G\,d_{\mathrm{h}}}{\mu_{\mathrm{l}}}$	Ratio of inertia to viscous forces. x is the vapour quality.
- Vapour Re_{v}	$Re_{\mathrm{v}} = \frac{G\,x\,d_{\mathrm{h}}}{\mu_{\mathrm{v}}}$	
Homogeneous Weber number We_{m}	$We_{\mathrm{m}} = \frac{G^2 d_{\mathrm{h}}}{\rho_{\mathrm{m}}\sigma}$	Ratio of inertia to surface tension forces. ρ_{m} is the mean density.
Reduced chevron angle	$\beta^* = \frac{\beta}{\beta_{\max}}$	$\beta_{\max} = 70°$ is the upper limit of eq. (17) and (18) validity.
Density ratio	$\rho^* = \frac{\rho_{\mathrm{l}}}{\rho_{\mathrm{v}}}$	
Bond number *Bd*	$Bd = \frac{g(\rho_{\mathrm{l}} - \rho_{\mathrm{v}})d_{\mathrm{h}}^2}{\sigma}$	$Bd = Co^{-2}$

https://doi.org/10.52202/077185-0108

2.3 Pressure drop

Pressure drop takes place in the heat exchanger core, the inlet and outlet. Ideally the core Δp should form the greatest possible fraction, to both efficiently convert allowed pressure drop to heat transfer improvement, and to minimize flow maldistribution. There are five main causes of pressure drop:

1. entry to the core – acceleration and irreversibilities of sudden contraction: $\Delta p_{\text{in}} = \Delta p_{\text{in,acc}} + \Delta p_{\text{in,irr}}$
2. friction (including form drag) at the heat transfer surface: Δp_{f}
3. gravity effects due to hydrostatic pressure change in vertical flow: Δp_{g}
4. momentum effects due to acceleration in the core due to density change: Δp_{mom}
5. exit from the core – deceleration and irreversibilities of sudden expansion: $\Delta p_{\text{out}} = \Delta p_{\text{out,dec}} + \Delta p_{\text{out,irr}}$

The core entry and exit pressure drops are evaluated with equations (19) and (20),

$$\Delta p_{\text{in}} = \frac{\rho_2 w_2^2}{2}\left[1 - \left(\frac{w_1}{w_2}\right)^2\right] + \frac{\rho w_1^2}{2} K_{\text{in}} = \frac{\rho_2 w_2^2}{2}[(1-\sigma^2) + \sigma^2 K_{\text{in}}], \tag{19}$$

$$\Delta p_{\text{out}} = \frac{\rho_3 w_3^2}{2}\left[1 - \left(\frac{w_3}{w_4}\right)^2\right] + \frac{\rho w_4^2}{2} K_{\text{out}} = \frac{\rho_3 w_3^2}{2}[(\sigma^2 - 1) + \sigma^2 K_{\text{out}}], \tag{20}$$

where σ is the ratio of port free-flow area to the core frontal area, and subscripts 1−4 refer to velocities just before and after core entry and exit, as shown in Fig.4. In the absence of correlations suitable for estimating accurate loss coefficients for the cases at hand, $K_{\text{port}} = K_{\text{in}} + K_{\text{out}} = 1.5$ is assumed according to Shah and Sekulic (2003), with the knowledge that this fails to account for some of the physical phenomena that affect the inlet port pressure drop. Lee *et al.* (2020) found outlet port pressure drops ca. 40−50% greater than in the inlet; port loss coefficients of $K_{\text{in}} = 0.6$ and $K_{\text{out}} = 0.9$ were thus used. Between inlet and outlet, core Δp for all elements i were evaluated with Eq. (21)−(23):

$$\Delta p_{\text{f,i}} = \frac{\bar{\rho}_{\text{i}} \overline{w}_i^2}{2} f_{\text{i}} L_{\text{i}}, \tag{21}$$

$$\Delta p_{\text{g}} = \bar{\rho}_{\text{i}} \Delta H_{\text{i}}, \tag{22}$$

$$\Delta p_{\text{mom,i}} = \frac{\bar{\rho}}{2}(\overline{w}_3^2 - \overline{w}_2^2) = \frac{\dot{m}}{2A_{\text{ff}}}(\overline{w}_3 - \overline{w}_2). \tag{23}$$

Single-phase friction factor f is obtained from eq. (13); two-phase f is based on Amalfi et al. (2016),

$$f = \left[33.36\left(\frac{\beta}{\beta_{\max}}\right)^{9.993} + 14.99\right] \cdot We_{\text{m}}^{-0.475} Bd^{0.255} \left(\frac{\rho_{\text{l}}}{\rho_{\text{v}}}\right)^{-0.571}, \tag{24}$$

where Weber and Bond numbers We_{m} and Bd are defined in Table 3.

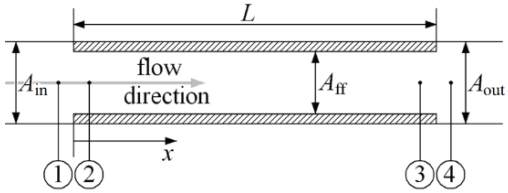

Figure 4: Locations and dimensions used in the following pressure drop analysis.

2.4 Calculation model

The combination of pentane work fluid and low-temperature, natural circulation system result in certain unique characteristic for the evaporator. Saturation pressure of pentane at considered temperature is very low at only 15 kPa(a). The hydrostatic pressure from a few meters of plate height is sufficient to sub-cool the pentane considerably, rendering the bottom part of the evaporator a liquid-liquid heat exchanger. As the pentane flows up in the heat exchanger and its temperature increases, eventually the

https://doi.org/10.52202/077185-0108

saturation temperature is reached, and boiling begins. From this point onwards, the pentane temperature starts to rapidly reduce, as the reduction of hydrostatic pressure reduces the saturation temperature further. The result is a highly unusual temperature profile, where the minimum temperature difference occurs not at the hot fluid exit as is typical in evaporators, but at the point where boiling begins, as shown in Fig.5. Parallel-flow arrangement presents no disadvantage with such temperature profile. The bottom part, where the subcooling due to downcomer hydrostatic pressure is removed, operates as a liquid-liquid heat exchanger. The height where the boiling begins is solved by starting with an initial guess for the height to onset of boiling, L_{OB}, and treating the error $\Delta T_{err} = T_{pent}(L_{OB}) - T_{sat}(p_{pent}(L_{OB}))$ as an objective function to minimize.

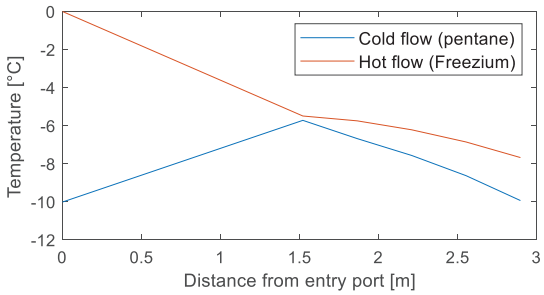

Figure 5: Temperature diagram of a low-pressure parallel-flow pentane evaporator.

While the liquid-liquid part can be calculated in a straightforward manner assuming constant overall heat transfer coefficient and properties and applying the effectiveness-NTU method, from L_{OB} upwards, the combination of small temperature differences and potentially non-linear behaviour could cause significant errors. Consequently, this part of the evaporator was evaluated in four calculation elements.

2.5 Optimization

Compared to shell-and-tube heat exchanger optimization, plate heat exchanger (PHX) optimization literature is sparse. Optimization studies of corrugated-plate evaporators are even fewer, although Imran *et al.* (2015) did minimize the cost and pressure drop by optimizing the L_{tot}, B_{tot} and $\hat{a}$ (see Fig.2) of an R245fa evaporator with a multi-objective genetic algorithm (GA). Most (PHX) optimization studies consider multi-objective optimization with a GA, typically minimizing pressure drop while maximizing heat transfer: either heat transfer coefficient (Najafi & Najafi 2010; Saleh *et al.*2013), heat transfer rate (Imran *et al.* 2017), or Nusselt number (Yicong *et al.*, 2023).

The problem of PHX optimization is multi-constrained, mixed-integer, non-differentiable and multi-modal. Stochastic metaheuristics are often used for such problems; the GA used in earlier studies is one such. In this work, the CS3/rand/1/bin cuckoo search variant (Saari *et al.*, 2022) was used. Like GA, it is a population-based method. It is based on the differential mutation from the differential evolution (DE) by Storn and Price (1997), augmented with Lévy-distributed random walks for robustness. Both search methods are capable of rotationally invariant search necessary for efficient performance on non-separable problems. This is an advantage over the GA variants, which tend to rely on crossover as a search method, resulting in inferior performance on non-separable problems (Saari *et al.*, 2019).

Fast, reliable convergence proved challenging to achieve compared to e.g. shell-and-tube heat exchanger optimization of similar dimensionality. Control parameter settings leaning heavily towards robustness over speed proved necessary, which together with the iterative multi-element thermohydraulic model led to long calculation times. Solution was sought, and found, from the use of a faster method for terminal convergence, taking advantage of the fact that the CS3 typically finds the approximate region of the solution relatively fast and spends then most of the run refining it. Once the probable region of the solution is found, the computationally heavy metaheuristic is no longer required, and search can be transferred to a faster deterministic search.

https://doi.org/10.52202/077185-0108

The Hooke-Jeeves (HJ) pattern search (Hooke & Jeeves, 1961) is a well-known deterministic direct method, but suffers from severely limited ability to search outside of the variable axes: such moves can only be sums of successful single-axis moves, which is problematic for a non-separable problems. To alleviate this, the possibility of diagonal moves was added to create a modified HJ algorithm (Alg.1).

Algorithm 1. Modified Hooke-Jeeves algorithm to minimize $f(\mathbf{x})$

```
begin
    n ← 0; set initial step length vector Δx_n ← (Δx_n,1, Δx_n,2, …, Δx_n,D)
    while number of function valuations < maximum and there exists Δx_n,d > minimum threshold
        f_n ← f(x_n); n ← n+1
        for all i = 1, …, D do                          // try moves in direction of each axis
            attempt moves by +/- Δx_n,i ;update x_n if succesful
        end for
        if x_n = x_n−1                                  // if no move was accepted
            reduce step size: Δx_n+1 ← ε Δx_n
            x_n = diagonal_exploration(x_n, Δx_n)
        else                                            // otherwise try pattern move
            attempt further pattern moves by the sum vector of all successful moves, until failure
        end if
    end while
end
begin function diagonal_exploration(x_n, Δx_n)
    for all i = 1, …, D-1 do
        for all j = i+1, …, D do
            attempt all 4 possible diagonal moves possible with ±Δx_n,i ± Δx_n,j
            if x_k,i+1 = x_k,i and j < D                // if two-axis moves fail, try three-axis moves
                for all k = j+1, …, D do
                    attempt all 8 possible diagonal moves possible with ±Δx_n,i ± Δx_n,j ± Δx_n,k
                end for
            end if
        end for
    end for
    if x_k,i+1 ≠ x_k,i
        attempt pattern moves until failure
    end if
end function
```

3 RESULTS AND DISCUSSION

The optimizer was run five times with a population size of 80, maximum number of iterations set at 2000, and crossover probability and Lévy flight scaling factors both set at 0.10; i.e., parameters leaning more towards robustness over speed than what was found sufficient with the same method earlier in (Saari *et al.*, 2022). This produced consistent convergence behavior. Calculation runs were slow, but not prohibitively so, typically finished overnight. By termination after 244 thousand objective function evaluations, the five runs had practically converged to the same solutions: the decision variables of the five results were all within 2% of each other, and objective function values within 0.1 percent. The convergence plot (objective function value against number of function evaluations) is shown in Fig.4; the best solution found is listed in Table 4.

At 3.7×1.8 meters, the optimized heat exchangers plates are very large, but not prohibitively so: plates of such size range are available from some manufacturers. The large size results from the combination of the unusual temperature profile and low overall heat transfer coefficient U of 330 W/m^{2}K.

The obtained cost should be considered as a tentative estimate at this point, due to considerable uncertainties in the estimation. Firstly, the reliability of cost correlation may reduce at the extreme high-end side of heat exchanger size, secondly, having pentane in sub-atmospheric, -0.85bar(g) pressure, may require additional costs to ensure no air leaks into the evaporator can create flammable mixture,

https://doi.org/10.52202/077185-0108

and finally, the cost estimation for additional parallel heat exchangers is still tentative and subject to considerable uncertainty at this point.

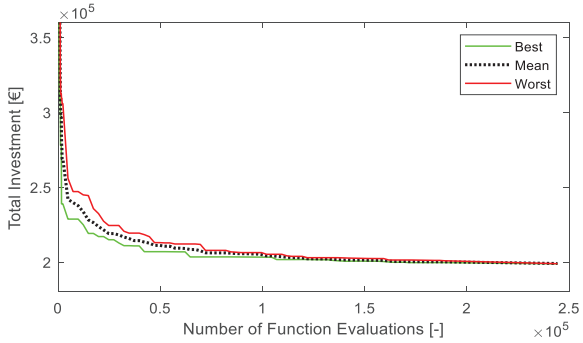

Figure 4: Convergence plots of five runs of optimization.

Table 4: Optimized decision variable values, and corresponding objective function value.

Variable	Explanation	Dimension	Best result	Considered range
x_1	Plate length, L_{tot}	[m]	3.68	$0.4 < x_1 < 3.8$
x_2	Plate width, B_{tot}	[m]	1.80	$0.1 < x_2 < 2.2$
x_3	Port diameter, fraction of plate width, $D_{\mathrm{p}}/B_{\mathrm{tot}}$	[-]	0.35	$0.1 < x_3 < 0.35$
x_4	Chevron angle, β	[°]	55	$25 < x_4 < 70$
x_5	Chevron wavelength (pitch), Λ	[mm]	22	$5.0 < x_5 < 50$
x_6	Chevron amplitude, ratio to pitch, $\frac{\Lambda}{\hat{a}}$	[-]	5.0	$2.0 < x_6 < 5.0$
x_7	Number of plates, N_{plt}	[-]	316	$50 < x_7 < 1000$
x_8	Number of parallel heat exchangers, N_{HX}	[-]	2	$1 < x_8 < 5$
$C_{\mathrm{DC,evap}}$	Total direct cost of installed evaporators	[10^3 €]	199	

Despite the uncertainties, the obtained results can nonetheless be considered an indication of probable economic feasibility. Average investment costs of large industrial heat pumps in Europe were typically in the order of 400 €/kW$_{\mathrm{th}}$ (Marina *et al.*, 2021), or 2 million for a 5 MW heat pump, in 2020. The obtained result of 10% of that cost for the evaporator unit appears unlikely to prove prohibitive.

As an optimization problem, the pentane evaporator optimization proved to be a challenging one. Compared to shell-and-tube heat exchanger optimization, there is little available literature on plate heat exchanger optimization, even less on evaporators. The multi-constrained, multi-modal, non-differentiable and non-separable characteristics of the problem require the use of a metaheuristic stochastic optimizer. A differential evolution – cuckoo search hybrid algorithm (Saari *et al.*, 2022) was used as the main optimizer. Reliable convergence proved challenging compared to shell-and-tube heat exchanger optimization of similar dimensionality, requiring control parameter settings leaning heavily towards robustness over speed. To improve performance, the population convergence is tracked during the run to allow switching from the stochastic global search to a faster, but local deterministic method when sufficient convergence could be observed. The Hooke-Jeeves search, modified to perform well on a non-separable problem, was used as the deterministic method.

4 SUMMARY AND CONCLUSIONS

In this work, a techno-economic optimization of a brazed-plate pentane evaporator for an industrial heat pump was conducted. Pentane was chosen as the work fluid through combination of requirements for

https://doi.org/10.52202/077185-0108

low environmental impact, and centrifugal compressor design constraints. Due to the very low pressure levels, a result of the low saturation pressure of pentane at the relevant temperature ranges, the saturation temperature is very sensitive to even small pressure changes. Consequently, as the boiling pentane flows through the heat exchanger, its temperature is reduced clearly, and minimum temperature difference occurs not at either end of the heat exchanger, but at the point where the boiling begins. This results in a temperature profile where there is little difference between parallel- and counter-flow configurations; in this work, parallel-flow configuration was considered.

In contrast to shell-and-tube heat exchanger optimization, the literature on the optimization of plate-type heat exchangers is limited, and mostly focuses on multi-objective optimization of liquid-liquid heat exchangers. Here the goal was to obtain an optimized design for the evaporator, however, and multi-objective optimization was thus ruled out in favor of cost minimization as the sole objective function. The decision variables used included evaporator size, surface geometry, and port diameters, as well as the possibility of installing more than one evaporator in parallel.

The optimized configuration was one of two parallel, 3.7×1.8 m heat exchangers with slightly over 300 plates each. While this is at the largest end of commercially available plate sizes, both the size and the estimated cost still appear to fall within potentially feasible range. Future research will be conducted to compare the results obtained with pentane to the possibility of using different work fluids less ideal for the compressor but more suitable for low-temperature evaporation. Within the topic of pentane cycle, future research will evaluate the possibility of evaporator size reduction through the use of a forced-circulation (pressurized) evaporator operating in a significantly subcooled region as a liquid-liquid heat exchanger, with a throttling valve and flash evaporation into drum after the heat exchanger. This would increase the flow velocity, and thus heat transfer coefficient, and in a counter-flow configuration the temperature profile would allow higher minimum temperature differences, especially using a sufficiently large pentane circulation number. In combination, these factors should permit clearly smaller heat exchangers.

5 REFERENCES

Amalfi, R.L., Vakili-Farahani, F. and Thome, J.R., 2016. Flow boiling and frictional pressure gradients in plate heat exchangers. Part 2: Comparison of literature methods to database and new prediction methods. *International Journal of Refrigeration*, *61*, pp.185-203.

Barbosa Jr, J.R., Cheah, L.W. and Hewitt, G.F., 2007. Flow boiling of water in a vertical tube at sub-atmospheric pressures. *Journal of the Brazilian Society of Mechanical Sciences and Engineering*, *29*, pp.401-409.

European Chemicals Agency. 2024. *Per- and polyfluoroalkyl substances (PFAS).* https://echa.europa.eu/hot-topics/perfluoroalkyl-chemicals-pfas (Accessed 23.2.2024)

European Commission. 2024. *EU legislation to control F-gases*. https://climate.ec.europa.eu/eu-action/fluorinated-greenhouse-gases/eu-legislation-control-f-gases_en (Accessed: 23.2.2024)

Hooke, R. and Jeeves, T.A., 1961. "Direct Search" Solution of Numerical and Statistical Problems. *Journal of the ACM (JACM)*, *8*(2), pp.212-229.

IEA. 2022. *The Future of Heat Pumps - World Energy Outlook Special Report*

Imran, M., Usman, M., Park, B.S., Kim, H.J., and Lee, D.H., 2015. Multi-objective optimization of evaporator of organic Rankine cycle (ORC) for low temperature geothermal heat source. *Applied Thermal Engineering*, 80, pp.1-9.

Imran, M., Pambudi, N.A., and Farooq, M., 2017. Thermal and hydraulic optimization of plate heat exchanger using multiobjective genetic algorithm. *Case studies in thermal engineering*, 10, pp.570-578.

Jaatinen-Värri, A., Honkatukia, J., Uusitalo, A., & Turunen-Saaresti, T., 2024. Centrifugal compressor design for high-temperature heat pumps. *Applied Thermal Engineering*, *239*, p. 122087.

Kakaç, S. ed., 1991. *Boilers, evaporators, and condensers*. John Wiley & Sons.

https://doi.org/10.52202/077185-0108

Kew, P.A., 1996. On pressure fluctuations during boiling in narrow channels. In *Proc. 2nd Eur. Thermal Sciences and 14th UIT Nat. Heat Transfer Conf., Rome, Italy, 1996* (pp. 1323-1327).

Kew, P.A. and Cornwell, K., 1997. Correlations for the prediction of boiling heat transfer in small-diameter channels. *Applied thermal engineering*, *17*(8-10), pp.705-715.

Lee, D., Song, K.S., Yun, S. and Kim, Y., 2020. Experimental evaluation of single-and two-phase pressure drops through inlet and outlet ports in a plate heat exchanger. *International Journal of Heat and Mass Transfer*, 158, p.120009.

Longo, G.A., Mancin, S., Righetti, G. and Zilio, C., 2015. A new model for refrigerant boiling inside Brazed Plate Heat Exchangers (BPHEs). *International Journal of Heat and Mass Transfer*, 91, pp.144-149.

Marina, A., Spoelstra, S., Zondag, H.A. and Wemmers, A.K., 2021. An estimation of the European industrial heat pump market potential. *Renewable and Sustainable Energy Reviews*, 139, p.110545.

Martin, H., 1996. A theoretical approach to predict the performance of chevron-type plate heat exchangers. *Chemical Engineering and Processing: Process Intensification*, 35, pp.301-310.

Martin, H., 2010, Pressure Drop and Heat Transfer in Plate Heat Exchangers, Chapter N6. *In: VDI Heat Atlas*, 2nd Ed., Springer: Berlin/Heidelberg, Germany: p. 1515

Martinez, C.M., Sermyagina, E., Saari, J., Ramos, V.F., Vakkilainen, E., Cardoso, M. and Rocha, E.P.A., 2023. Fast oxidative pyrolysis of eucalyptus wood residues to replace fossil oil in pulp industry. *Energy*, *263*, p.126076.

Müller-Steinhagen, H. Fouling of Heat Exchanger Surfaces, Chapter C4. *In: VDI Heat Atlas*, 2nd Ed., Springer: Berlin/Heidelberg, Germany: p. 83

Najafi, H. and Najafi, B., 2010. Multi-objective optimization of a plate and frame heat exchanger via genetic algorithm. *Heat and mass transfer*, 46, pp.639-647.

Roetzel, W., Luo, X. and Chen, D., 2019. *Design and operation of heat exchangers and their networks*. Academic Press.

Saari, J., García Perez, M., Vianna Neto, M., Cardoso, M., Vakkilainen, E. and Kaikko, J., 2019. Shell-and-tube heat exchanger optimization-impact of problem formulation and cost function. *Proceedings HEFAT 2019 14th International Conference on Heat Transfer, Fluid Mechanics and Thermodynamics*, HEFAT: pp. 1350-1356.

Saari, J., Martinez, C.M., Kaikko, J., Sermyagina, E., Mankonen, A. and Vakkilainen, E., 2022. Techno-economic optimization of a district heat condenser in a small cogeneration plant with a novel greedy cuckoo search. *Energy*, 239, p.122622.

Saleh, K., Aute, V., Radermacher, R. and Azarm, S., 2013. Chevron plate heat exchanger optimization using efficient approximation-assisted multi-objective optimization techniques. *HVAC&R Research*, 19(7), pp.788-799.

Shah, R.K., Sekulić, D.P., 2003, *Fundamentals of Heat Exchanger Design and Manufacture*, John Wiley & Sons: Hoboken, NJ, USA: p. 514.

Statistics Finland. *Producer price indices*. [Online: accessed Jan 5th, 2024] Available: https://pxdata.stat.fi/PxWeb/pxweb/fi/StatFin/StatFin__thi/statfin_thi_pxt_118g.px

Storn, R., and Price, K., 1997. Differential evolution–a simple and efficient heuristic for global optimization over continuous spaces. Journal of global optimization, 11, pp.341-359.

Yicong, L., Chunyu, S., Wei, L. and Zhichun, L., 2023. Structural parameter design of welded plate heat exchanger based on multi-objective optimization algorithm. *International Communications in Heat and Mass Transfer*, 146, p.106900.

6 ACKNOWLEDGEMENT

This work received financial support from Business Finland under research project ”NEXTHEPS - Development of Next Generation Large Scale Heat Pump Systems (grant number: 1535/31/2022)”

https://doi.org/10.52202/077185-0108